Research Square

Preprints are preliminary reports that have not undergone peer review.
They should not be considered conclusive, used to inform clinical practice,
or referenced by the media as validated information.

Eggshell-derived mineral and membrane fillers in a cold-cured PMMA matrix: phase transformation, local nanomechanics and multiscale mechanical response

Iasmina-Mădălina Petculescu
Politehnica University of Timișoara
Carmen Opriș
Politehnica University of Timișoara
Dragoș Buzdugan
Politehnica University of Timișoara
Maria Rada
"Victor Babes" University of Medicine and Pharmacy
Ion-Dragoș Uțu
Politehnica University of Timișoara
Alexandru-Viorel Coșa
alexandru.cosa@upt.ro

Politehnica University of Timișoara

Article

Keywords: Eggshell, Calcination, PMMA matrix, Particulate composite Nanoindentation Porosity

Posted Date: November 4th, 2026

DOI: https://doi.org/10.21203/rs.3.rs-11305779/v1

License: This work is licensed under a Creative Commons Attribution 4.0 International License.
Read Full License

Additional Declarations: No competing interests reported.

Eggshell-derived mineral and membrane fillers in a cold-cured PMMA matrix: phase transformation, local nanomechanics and multiscale mechanical response

Iasmina-Mădălina Petculescu[a], Carmen Opriș[a], Dragoș Buzdugan[a], Maria Rada[b], Ion-Dragoș Uțu[a], Alexandru-Viorel Coșa[a,*]

[a] Department of Materials Science and Manufacturing, Faculty of Mechanical Engineering, Politehnica University of Timișoara, Bd. Mihai Viteazu 1, 300222 Timișoara, Romania
iasmina.petculescu@upt.ro, carmen.opris@upt.ro, dragos.buzdugan@upt.ro, dragos.utu@upt.ro
[b] Cardiology Department, "Victor Babes" University of Medicine and Pharmacy, Eftimie Murgu Square 2, 300041, Timișoara, Romania, rada.maria@umft.ro
* Corresponding author: e-mail address: alexandru.cosa@upt.ro

Acknowledgements

The authors acknowledge the Laboratory of Mechanics and Strength of Materials, Faculty of Mechanical Engineering, Politehnica University of Timișoara, for access to the mechanical testing equipment and Giosan Calin for support in performing the tests.

Abstract

Cold-cured poly(methyl methacrylate) is used for prosthetic, dental and repair components, where the stiffness of the resin is adequate while notch sensitivity and low energy absorption limit service. Hen eggshell is a waste generated in very large quantities and an attractive particulate filler for such systems. Native eggshell mineral (ES), the same mineral calcined at 900 °C for 3 h (CES) and the separated membrane (ESM), all from one batch of shells, were cast into a cold-cured acrylic at 5, 10 and 15 wt% mineral and 1, 2.5 and 5 wt% membrane. Calcination converted calcite to CaO that partly rehydrated to portlandite and lowered the indentation modulus of the filler-associated regions from 33.0 to 8.3 GPa and raised the apparent porosity of the 15 wt% composite from 1.3 to 7.3%. Every filled formulation was stiffer in tension than the matrix, by 19–67%, and at 15 wt% the calcined composites were stiffer than the native ones despite their more compliant filler and higher porosity. Tensile strength stayed within 1.01–1.29 times the Nicolais–Narkis prediction for non-adhering inclusions. Flexural strength fell to 39–55% of the reference, while compressive yield stress was retained.

Keywords Eggshell, Calcination, PMMA matrix, Particulate composite Nanoindentation Porosity

1. Introduction

Waste management of food-processing residues is a persistent environmental problem and hen eggshell is one of its largest single contributors. Several million tonnes of eggshell are discarded annually [1], most of it to landfill, where the adhering organic matter makes disposal costly [2]. About 94 % of the shell is calcium carbonate in the calcite form, the remainder being magnesium carbonate, calcium phosphate and an organic fraction [3]. The waste is therefore a widely available and almost free source of mineral filler [1, 4], and it has been examined as a catalyst support, as a precursor for hydroxyapatite and bone cements, as a partial replacement for cement and as a particulate filler in polymers [5, 6].

In polymer systems, eggshell powder has been incorporated into polypropylene [7], polyethylene [8], poly(vinyl chloride) [9], poly(lactic acid) [10], poly(vinyl alcohol) [11],

polycaprolactone [12], natural and nitrile rubbers [13, 14], epoxy [12, 15] and unsaturated polyester matrices [16]. Across these systems the elastic modulus commonly increases at low to moderate loading as Owuamanam and Cree have observed [2, 10]. Strength and ductility follow a far less consistent trajectory and frequently deteriorate once a critical content is exceeded. Agglomeration, incomplete wetting and weak adhesion between the mineral surface and a comparatively hydrophobic polymer are the explanations usually offered [2, 9, 13]. The same divergence is visible in the reported optimum filler contents, which range from below 5 wt% to above 30 wt% depending on the matrix, on particle size and on the processing technology [10, 17–21].

Particulate-composite theory describes this behaviour well. Elastic stiffness is governed mainly by the volume fraction, geometry and modulus contrast of the inclusions and is comparatively insensitive to the quality of the interface [22, 23]. Ultimate strength depends directly on whether stress can be transferred across that interface [24–27]. In the limiting case of zero adhesion, the particles behave as voids, a situation described by the Nicolais-Narkis expression [28, 29]. A rigid mineral inclusion can therefore raise the modulus of a polymer while lowering its strength, and the two observations are perfectly compatible.

Cold-cured poly(methyl methacrylate) (PMMA) is a relevant host for such fillers because it polymerizes at ambient temperature within minutes and is cast in place for prosthetic, orthotic, dental and repair components [30, 31]. The filler therefore enters a fast, low-viscosity process in which moisture, surface chemistry and entrapped air are never removed by a later step. In service the cured resin is limited by notch sensitivity and low energy absorption, while its stiffness is usually adequate. Eggshell powder, raw or burned, has already been shown to modify the strength and stiffness of self-curing acrylics [30, 32]. Those studies varied concentration and burn state only. The present work adds the membrane as a co-filler, a defined calcination with identification of the resulting phases, nanomechanics of the filler-associated regions and the effect of the calcined filler on the porosity of the cast part.

Calcination provides a controlled way to alter the filler itself. At about 900 °C, $CaCO_3$ decomposes to CaO, while subsequent exposure to moisture can produce $Ca(OH)_2$ (portlandite) [5, 6]. The product differs from native calcite in phase composition, morphology, porosity and moisture sensitivity, and in a cast-in-place resin a reactive, hygroscopic filler also raises the question of how it affects the product. The eggshell membrane provides a second, chemically distinct fraction, as it is a protein-rich fibrous network that is normally discarded during shell processing [3] and has been shown to remain mechanically active after separation and grinding [33, 34]. The two fractions therefore offer a stiff mineral and a compliant organic filler from the same waste stream without an external synthetic coupling agent.

This study investigates three eggshell-derived fillers obtained from a single batch of hen eggshells: native mineral powder (ES), mineral powder calcined at 900 °C for 3 h (CES), and separated, untreated eggshell membrane (ESM). ES and CES were incorporated at 5, 10 and 15 wt%, while ESM was added at 1, 2.5 and 5 wt% to the formulations containing 15 wt% mineral filler. The designation CESM refers to the combination of CES with untreated ESM. XRD, SEM/EDS and nanoindentation were combined with tensile, flexural and compression testing, density-based apparent porosity measurements and the Guth and Nicolais–Narkis reference models. The questions addressed are whether the state of the eggshell-derived filler controls bulk mechanics through changes in phase, morphology and local nanomechanics, and whether the particles transfer meaningful stress across the interface and which preparation is preferable.

2. Materials and Methods

2.1. Matrix

The polymer matrix used was Technovit 4004 (Kulzer GmbH, Hanau, Germany) [35], a two-component cold-curing acrylic consisting of a PMMA powder with peroxide initiator and a methyl methacrylate liquid with amine activator. These are called the PMMA powder and the monomer liquid below, to distinguish them from the eggshell fillers. The PMMA powder-to-monomer liquid mass ratio was fixed at 2:1 for all formulations, and polymerization was complete about 4–6 min after mixing.

2.2. Preparation of the eggshell-derived fillers

Hen eggshells from one waste stream were washed, emptied of residual contents and rinsed with distilled water. The inner membrane was manually separated from the mineral shell and both fractions were washed separately and dried at room temperature for 48 h, so that neither the calcite nor the protein was thermally modified. The dried mineral and membrane were ground separately in a household electric grinder to visually homogeneous powders and were not sieved. The native mineral was designated ES and the membrane ESM (as seen in Fig. 1).



Fig. 1 Preparation of the eggshell-derived powders: separation of the mineral shell and of the membrane, washing, drying and grinding to ES and ESM

Only the mineral eggshell powder (ES) was calcined. It was placed in a cold laboratory furnace, heated to 900 °C and maintained at this temperature for 3 h. The resulting powder was designated CES. The separated eggshell membrane (ESM) was not subjected to calcination. The designation CESM refers to the combination of calcined mineral powder (CES) with untreated membrane (ESM), rather than to a separately calcined membrane powder. SEM and XRD analyses focused on ES and CES to assess the morphological and phase changes induced by calcination; the CES–ESM combination was not characterized separately by these techniques.

2.3. Composite preparation

The fillers were weighed for each formulation and mixed mechanically with the PMMA powder and the liquid monomer, and the mixture was placed on a vibration table while casting to release entrapped air. All filler contents are weight percentages of the total cured composite mass, that is, of PMMA powder, monomer liquid and filler. The thirteen formulations are given in Table 1 and the steps are presented in Fig. 2.



Fig. 2 Mixing sequence of Technovit 4004 with the eggshell-derived fillers (ES, CES, ESM and CESM). Mould casting, demoulding, mechanical finishing and the final composite specimens

Table 1 Designation and composition of the investigated formulations

Designation	Mineral filler	Mineral (wt%)	Mineral (vol%)[a]	Membrane (wt%)	Total filler (vol%)[a]
REF - Resin	none	0	0	0	0
ES5	ES (native)	5	2.2	0	2.2
ES10	ES (native)	10	4.6	0	4.6
ES15	ES (native)	15	7.1	0	7.1
ES15/M1	ES (native)	15	7.1	1	8.1
ES15/M2.5	ES (native)	15	7.2	2.5	9.6
ES15/M5	ES (native)	15	7.2	5	12.2
CES5	CES (900°C)	5	1.8	0	1.8
CES10	CES (900°C)	10	3.8	0	3.8
CES15	CES (900°C)	15	5.9	0	5.9
CES15/M1	CES (900°C)	15	5.9	1	6.9
CES15/M2.5	CES (900°C)	15	5.9	2.5	8.4
CES15/M5	CES (900°C)	15	5.9	5	10.9

[a]Volume fractions were calculated from the mass fractions using densities of 1.18 g cm^{-3} for the cured matrix, 2.71 g cm^{-3} for calcite, 3.35 g cm^{-3} for calcium oxide and 1.30 g cm^{-3} for the membrane.

At a matched mass fraction of 15 wt%, CES occupies 5.9 vol% against 7.1 vol% for ES, because the calcined mineral is denser than calcite. The two mineral series are consequently not iso-volumetric at equal mass fraction.

2.4. Structural and chemical characterisation

2.4.1. X-ray diffraction (XRD)

XRD was performed on ES, CES and ESM with a PANalytical X'Pert PRO diffractometer using Cu Kα radiation (λ = 1.540598 Å) over a 2θ range of ~ 5.01–79.99° with a 0.02° step.

Phases were identified against ICDD reference patterns for calcite (PDF 47-1743), CaO (PDF 37-1497) and $Ca(OH)_2$ (PDF 44-1481). XRD and SEM analyses were performed on ES, CES and untreated ESM to characterize the individual filler constituents. The CES–ESM combination, designated CESM, was not examined separately, as its constituents were characterized individually. Consequently, these analyses do not establish whether combining CES with ESM produces additional morphological or phase changes.

2.4.2. Scanning electron microscopy (SEM)

SEM/EDS (done on a FEI Inspect S equipment at 15 kV and 10 mm working distance) was used to examine powder morphology, elemental distributions, particle–matrix contact, agglomeration and fracture surfaces. Specimens were gold coated before observation. Particle dimensions were read from representative fields and are descriptive, since no particle-size distribution was measured.

2.5. Nanoindentation

Instrumented nanoindentation was performed according to ISO 14577 on polished cross-sections with an Anton Paar NHT STEP 500 nanoindenter and a Berkovich diamond indenter. The specimens were loaded at 100 mN min^{-1} to 5 mN, held for 20 s and unloaded at 50 mN min^{-1}. Indentation hardness and indentation modulus were obtained using the Oliver–Pharr method [36]. Five indents were made on each of five target formulations: unfilled resin and filler-associated regions in ES, ESM, CES and CESM.

2.6. Mechanical testing

Mechanical tests were performed at 23 ± 2 °C after at least 88 h of conditioning, so that post-cure and moisture uptake had stabilised; the moisture taken up by CES in this period belongs to the tested material state. The programme was nested: thirteen formulations were tested in tension, nine in flexure and seven in compression, and every formulation of a reduced campaign was also tested in all broader ones. All powders came from a single batch of shells, which excluded batch-to-batch biological variation and fixed the filler quantity. Calcination removes 44% of the carbonate mass as CO_2, and the hand-separated membrane was the scarcest fraction, so the membrane levels were crossed only with 15 wt% mineral. Tension, the loading state most sensitive to debonding, served as the screen over the full matrix. Flexure kept the reference, the native loading and membrane series, CES15 and CES15/M2.5. Compression, the test least sensitive to the interface, was concentrated on the reference and six 15 wt% formulations, where the porosity contrast between the formulations was expected to be largest.

2.6.1. Tensile testing

Tensile properties were determined on a Zwick Z005 machine (with a 5 kN load cell) according to ISO 527-1/-2 using type 1A specimens. The nominal geometry was 170 × 10 × 4 mm. Tensile modulus was the 0.05–0.25% chord at 1 mm min^{-1}, followed by 5 mm min^{-1} for strength and strain was measured with an extensometer with 30 mm gauge length. Energy to fracture was obtained with the trapezoidal rule to get the area under the stress–strain curve.

Tensile stress was referred to the measured initial cross-section of each specimen:

$$\sigma = F/A_0, \quad (1)$$

$$where\ A_0 = b \cdot h$$

and the strain to its gauge length:

$$\varepsilon = \Delta L / L_0 \quad (2)$$

The tensile modulus was taken as the chord between the two conventional strain levels of ISO 527-1, using:

$$E = (\sigma_2 - \sigma_1)/(\varepsilon_2 - \varepsilon_1), \quad (3)$$

$$\varepsilon_1 = 0.0005,$$

$$\varepsilon_2 = 0.0025$$

2.6.2. Three-point bending

Three-point bending was performed according to ISO 178 on a Metrotec system with a 1 kN load cell, 64 mm support span and 2 mm min^{-1} test speed. Specimens were 10 × 4 mm nominally. Flexural modulus was obtained from the 0.05–0.25% chord using crosshead displacement and is therefore used only for within-study comparison. Flexural strength, strain at fracture and nominal absorbed energy were calculated from the recorded curves.

$$\sigma_f = 3\,F\,L\,/\,(2\,b\,h^2) \quad (4)$$

$$\varepsilon_f = 6sh/L^2 \quad (5)$$

where L is the support span, s is the deflection at mid-span and ε_f is the strain at fracture. With the flexural modulus taken as the chord between the same two strain levels:

$$E_f = (\sigma_{f2} - \sigma_{f1})\,/\,(\varepsilon_{f2} - \varepsilon_{f1}) \quad (6)$$

The area under the nominal flexural stress–strain curve up to the fracture point, EA_{tot}, was obtained by trapezoidal integration of the recorded data. Because the bending stress is not uniform through the section, EA_{tot} is a nominal energy density used for comparison between formulations, not a true volumetric fracture energy.

$$EA_{tot} = \sum_{i=1}^{n-1} \frac{\sigma_i + \sigma_{i+1}}{2} \cdot (\varepsilon_{i+1} - \varepsilon_i) \quad (7)$$

2.6.3. Compression

Compression performance was evaluated according to ISO 604 on 12.5 mm diameter × 25 mm cylinders at 5 mm min^{-1}. Compressive stress used the measured initial section and yield stress was defined as the first local maximum. Compressive modulus was taken over 0.5–1.5% nominal strain, and energy to yield was integrated from the stress–deformation curve. The density cylinders were also used for apparent porosity determination.

Compressive stress and deformation were referred to the measured initial dimensions of each cylinder:

$$\sigma_C = F\,/\,A_0 \quad (8)$$

$$\varepsilon_c = \Delta h/h_0 \quad (9)$$

2.6.4. Density and porosity

Bulk density was obtained from cylinder mass and measured volume. Theoretical density was calculated from the rule of mixtures using the component densities listed in Table 1. Apparent porosity was the density deficit relative to that theoretical value. Because CES contains reactive CaO that partially hydrates, the result depends on the assumed component densities and is therefore called apparent porosity.

The bulk density of each cylinder followed from its mass and its measured geometry:

$$\rho = 4m/(\pi d^2 h) \quad (10)$$

where m is the specimen mass, d the diameter and h the height. The theoretical density followed from the rule of mixtures:

$$1/\rho_t h = \Sigma(w_i/\rho_i)) \tag{11}$$

where $w_i \; and \; \rho_i$ are the mass fraction and the density of component i. The porosity was obtained from the deviation between the two:

$$P = (1 - \rho/\rho_t h) \cdot 100 \tag{12}$$

where P is expressed in percent.

2.6.5. Statistical analysis

Results are reported as mean ± standard deviation. Three specimens per formulation were planned for each test and the statistics use the conclusive tests only. Because the formulation matrix is nested, a single three-factor analysis cannot be fitted. Two-factor ANOVA with type III sums of squares was applied to the supported sub-designs: mineral state × mineral loading without membrane (design A, tension), mineral state × membrane content at 15 wt% mineral (design B, tension) and the reduced 2 × 2 designs at 0 and 2.5 wt% membrane for flexure (C) and compression (D). Each campaign was also analysed by one-way ANOVA with Tukey–Kramer post hoc testing; $p < 0.05$ was considered significant, partial η^2 is reported as effect size, and the two-factor results are collected in Section 3.8. Claude (Anthropic) was used to assist with language editing, with the preparation of the statistical analysis scripts (run in Python with SciPy) and with checking the data processing; the authors reviewed and edited all outputs and take full responsibility for the content.

3. Results and discussion

3.1. Filler morphology and elemental composition

SEM showed a clear morphology change after calcination (Fig. 3). Native ES consisted of compact, irregular fragments, whereas CES was more fragmented, rough and granular, with porous secondary aggregates. Calcination therefore breaks up the shell structure and re-agglomerates the finer, rougher products. Representative projected dimensions in the analysed fields were about 50 to 80 µm for finer fragments and 300 to 480 µm for larger fragments in ES and 190–310 µm for CES aggregates. ESM retained a distinct fibrous, sheet-like architecture.

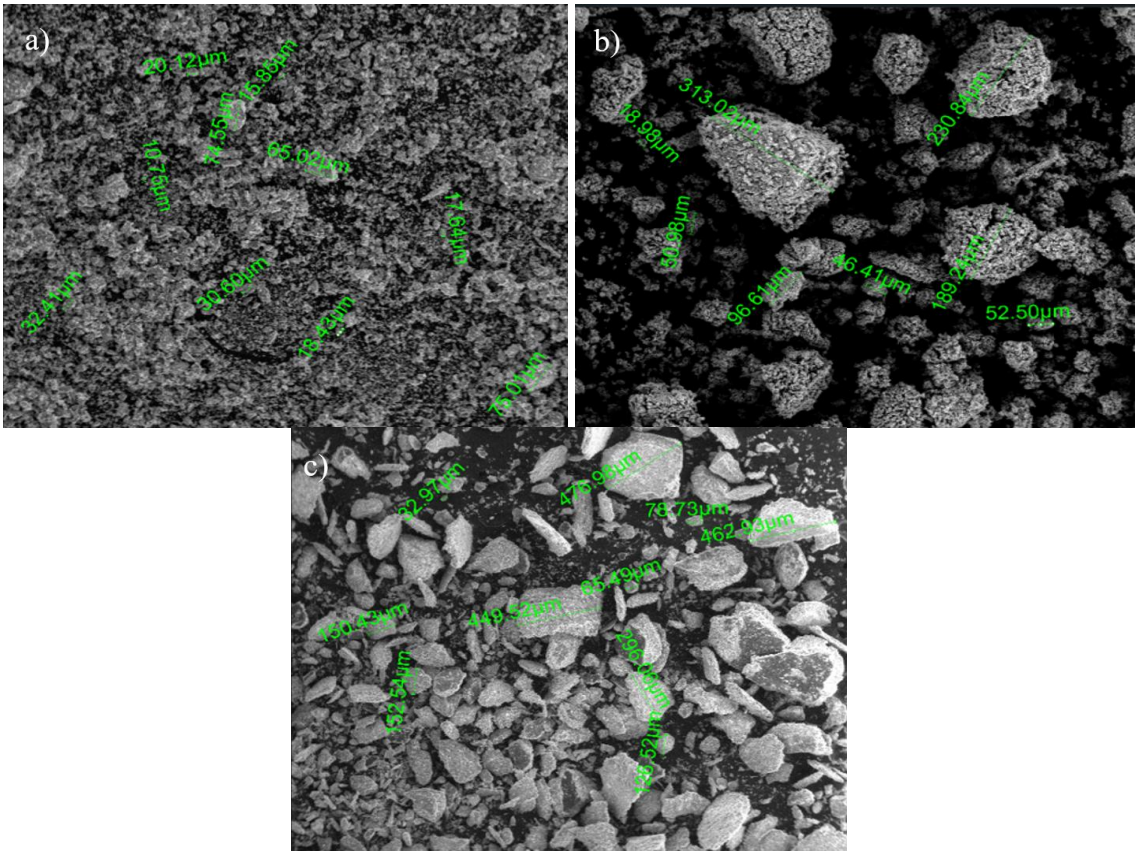


Fig. 3 Comparative SEM micrographs of the investigated powders: (a) native eggshell powder (ES), (b) calcined eggshell powder (CES) and (c) dried and ground eggshell membrane (ESM)

EDS mapping (Fig. 4) distinguished the mineral and membrane fractions. ES showed overlapping C, O and Ca distributions, CES showed a stronger relative Ca contribution and reduced C signal, and ESM was dominated by C and O with sparse Ca-rich features. The spectra are shown in Fig. 5 and the semi-quantitative compositions in Table 2.

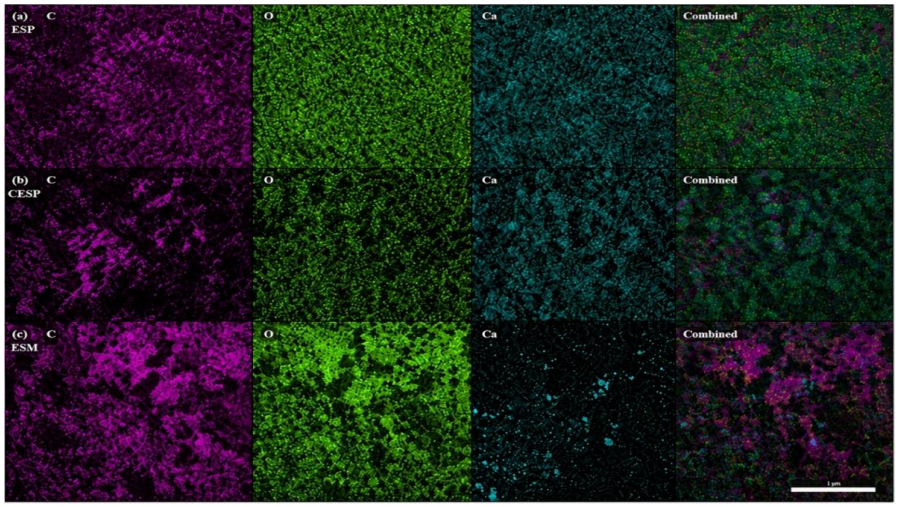


Fig. 4 EDX elemental mapping of (a) ES, (b) CES and (c) ESM, showing the individual C, O and Ca distributions and the combined map

For ES, pronounced C and O signals were observed together with a clear Ca peak, reflecting the mineral-rich composition of the untreated eggshell powder. After calcination at 900°C, the

CES spectrum exhibited a more pronounced Ca signal relative to C, indicating a change in the elemental composition of the analyzed region following thermal treatment. In contrast, the ESM spectrum was dominated by C and O, while the Ca signal was considerably less pronounced, consistent with the predominantly organic nature of the eggshell membrane.

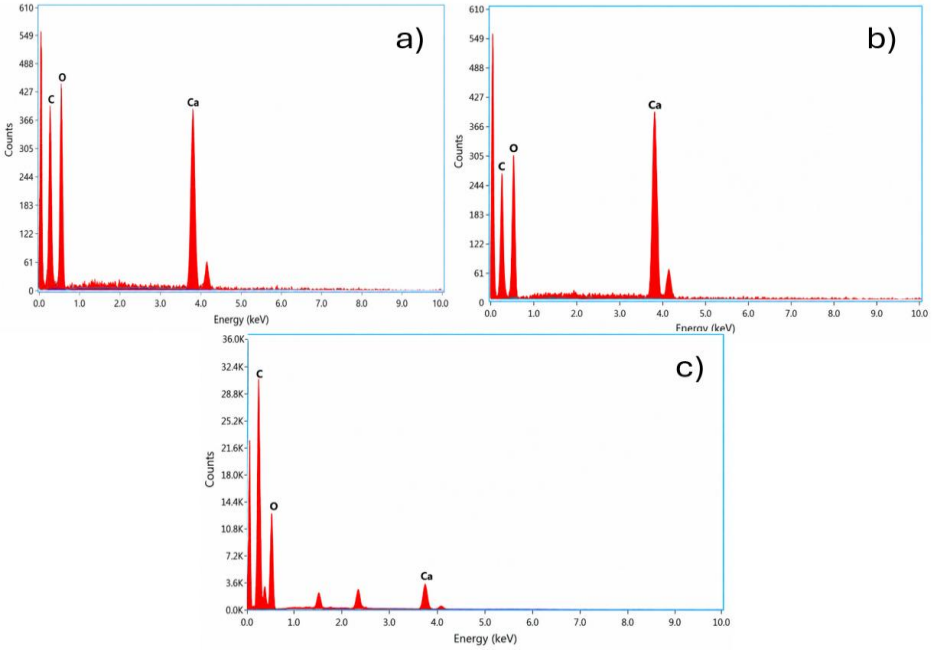


Fig. 5 EDX spectra of (a) ES, (b) CES and (c) ESM. Only the spectra are displayed for visual comparison; the quantitative results are discussed in the text

Because EDS is local and semi-quantitative, the values in Table 2 are read as trends. The carbon measured on ES (24.0 wt%, against 12.0 wt% for stoichiometric calcite) and on CES, in which XRD detects no calcite, includes adventitious carbon and a contribution of the carbon support, and the Ca content of CES (43.8 wt%) lies below that of CaO (71.5 wt%) and $Ca(OH)_2$ (54.1 wt%). Phase conversion is therefore established from XRD.

Table 2 Elemental composition of ES, CES and ESM determined by EDX analysis

Sample	C (wt%)	O (wt%)	Ca (wt%)
ES	23.96	45.59	30.46
CES	18.76	37.44	43.80
ESM	55.15	41.54	3.31

3.2. Phase composition

XRD patterns are shown in Fig. 6. ES and ESM contained calcite as the dominant crystalline phase, the membrane retaining some residual mineral after separation. In CES the calcite reflections disappeared and new reflections of CaO and $Ca(OH)_2$ appeared. Calcination thus decomposed the carbonate, and the oxide partially rehydrated to portlandite during cooling, handling and storage:

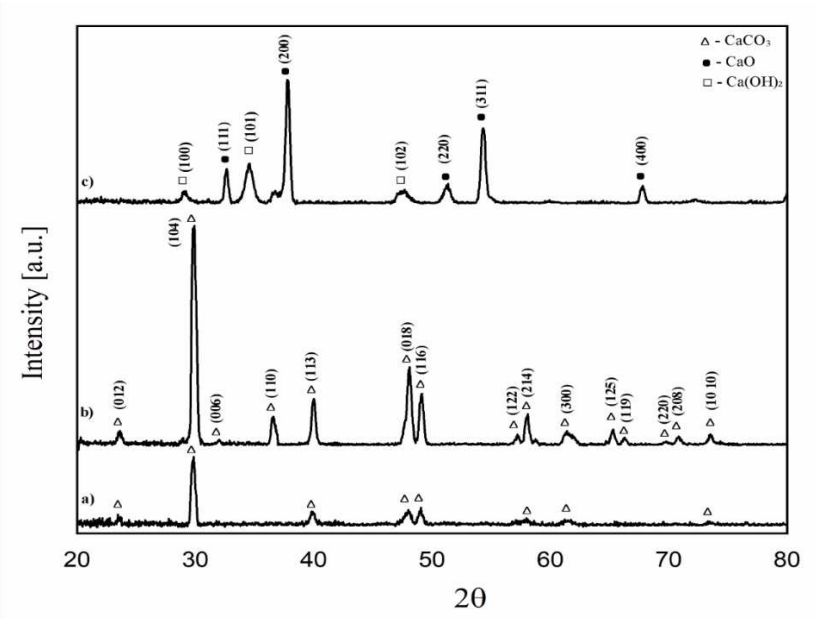


Fig. 6 X-ray diffraction patterns of (a) ESM, (b) ES and (c) CES, with indexed reflections and phase labels

The diffraction patterns of both ESM and ES exhibited the characteristic reflections of calcite ($CaCO_3$), indicating that calcium carbonate remained the dominant crystalline phase in the untreated eggshell-derived materials. The ES pattern showed sharp and intense diffraction peaks, confirming the highly crystalline nature of the native eggshell mineral fraction. Although ESM is primarily an organic material, the diffraction pattern revealed the presence of the same calcite phase, indicating that residual mineral constituents remained associated with the membrane after separation and processing.

A substantial phase transformation occurred after calcination at 900°C. The diffraction pattern of CES differed markedly from those of ESM and ES, with the disappearance of the characteristic calcite reflections and the appearance of new peaks associated with calcium oxide (CaO) and calcium hydroxide ($Ca(OH)_2$). These results confirm the decomposition of calcium carbonate during thermal treatment according to:

$$CaCO_3 \rightarrow CaO + CO_2 \tag{13}$$

The presence of CaO demonstrates successful calcination of the eggshell powder and conversion of the original carbonate-rich mineral phase into a reactive oxide phase. In addition to CaO, reflections attributable to portlandite, $Ca(OH)_2$, were observed. The appearance of this phase indicates partial hydration of calcium oxide after calcination. This behaviour is expected because CaO is highly hygroscopic and readily reacts with atmospheric moisture during cooling, handling and storage according to:

$$CaO + H_2O \rightarrow Ca(OH)_2 \tag{14}$$

The diffraction peaks of portlandite confirm that hydration occurred after thermal treatment. These phase transformations are particularly important for understanding the subsequent microstructural and mechanical behaviour of the composites. While ESM and ES contain calcite as the dominant crystalline constituent, calcination generates a fundamentally different mineral system characterized by the presence of CaO and its hydration products.

3.3. Composite microstructure and fracture behaviour

SEM micrographs were used to assess mineral incorporation into the matrix, particle–matrix contact and possible agglomeration, focusing on morphology relevant to load transfer and mechanical behaviour rather than membrane identification. All images were acquired at 5000× with a 20 µm scale bar and are shown in Fig. 7 (ES) and Fig. 8 (CES). The approximately 25 µm-wide field is small relative to the particles, so the images reveal local contact conditions rather than overall filler distribution.

ES15, the reference for the untreated-eggshell series, shows large, compact mineral fragments with distinct boundaries and heterogeneous surface relief. Matrix contact is visible, although the compact surfaces provide limited opportunities for mechanical anchoring.

With 1% membrane, ES15/M1 shows greater surface continuity and less distinct boundaries between compact regions. No extensive particle–matrix gaps are visible in the examined field, suggesting close contact between components.

At 2.5% membrane, ES15/M2.5 displays compact regions alongside rougher, lamellar areas, with extensive but irregular contact. The greater heterogeneity compared with ES15/M1 suggests changes in particle incorporation rather than a simple increase in structural uniformity.

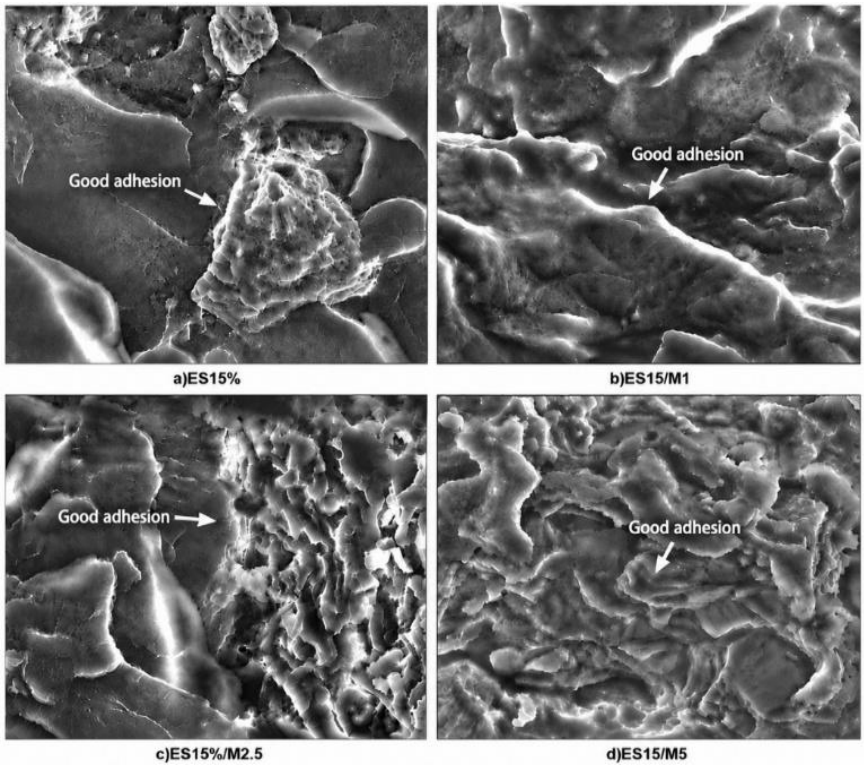


Fig. 7 SEM micrographs of the composites containing 15 wt% untreated eggshell: ES15, ES15/M1, ES15/M2.5 and ES15/M5

For ES15/M5, the microstructure becomes visibly denser and more layered, with numerous overlapping lamellar features and locally agglomerated regions. Local contact between the components is still present, but the distribution is less uniform.

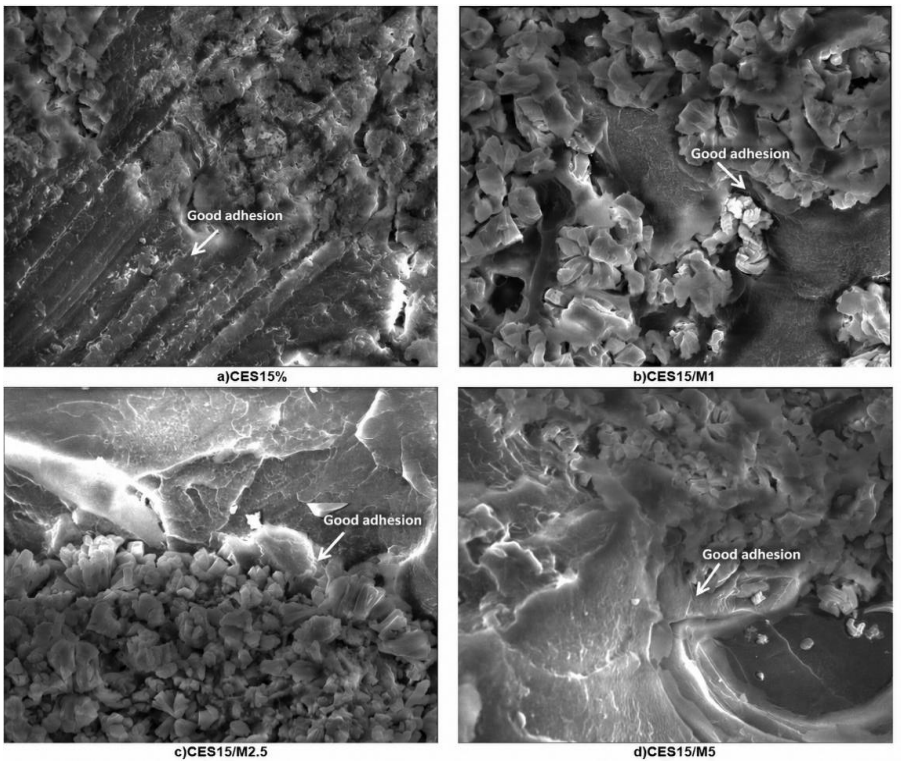


Fig. 8 SEM micrographs of the composites containing 15 wt% calcined eggshell: CES15, CES15/M1, CES15/M2.5 and CES15/M5

CES15 shows the morphological effect of calcination: compared with ES15, the mineral phase contains smaller, more angular fragments with rougher surfaces, providing more edges and irregularities for matrix contact.

In CES15/M1, fine particles surround continuous matrix regions, with close contact and no large, continuous interfacial gaps in the observed field. CES15/M2.5 shows numerous fragments of different sizes embedded in a continuous structure, creating an extensive, irregular particle–matrix interface.

This close contact does not correspond to a measurable improvement in mechanical performance. CES15/M2.5 reaches tensile and flexural strengths of 28.2 and 38.7 MPa, respectively, indistinguishable from CES15 within the measured scatter. Its compressive yield stress of 106.6 MPa also falls within the range of the other formulations. Together with the Nicolais–Narkis comparison in Section 3.10, these results indicate that the observed embedding does not establish effective interfacial stress transfer.

In CES15/M5, substantial particle–matrix contact remains, but dense particle accumulations alternate with more continuous regions. This less uniform arrangement may produce local differences in stiffness.

Overall, ES15 retains larger, compact mineral regions, whereas CES15 contains smaller, rougher fragments and aggregates. Membrane addition modifies their local arrangement, with greater heterogeneity at the highest content. SEM reveals contact, fragmentation, roughness, voids and agglomeration, but does not establish chemical bonding or adhesion; the interpretation therefore rests on observable morphology.

SEM analysis of tensile fracture surfaces (Fig. 9) compares REF with the ES15 and CES15 series at 0, 1, 2.5 and 5% membrane to assess changes in fracture behaviour. The analysis considers surface roughness, crack paths, agglomeration, pores, particle detachment and the appearance of the particle–matrix interface.

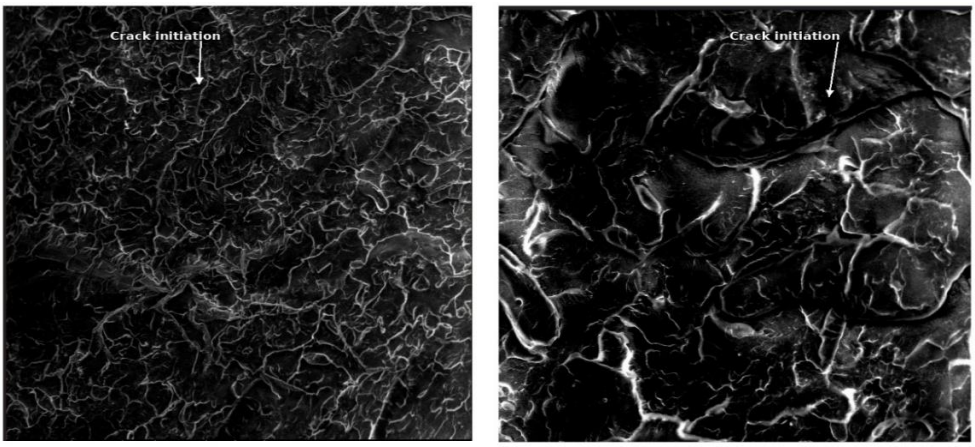


Fig. 9 SEM morphology of the fracture surface of the unfilled reference

REF exhibits a rough fracture surface with ridges, steps and branching fracture lines (Fig. 9). The tortuous crack path suggests predominantly brittle fracture with localized matrix deformation, without evidence of extensive plasticity. As no filler is present, isolated cavities are attributed to pores or trapped air rather than particle pull-out. These defects may concentrate stress and initiate cracks, which subsequently propagate through locally weaker regions of the matrix.

Adding 15% untreated eggshell powder produces a more heterogeneous fracture surface (Fig. 10). Particles obstruct and deflect cracks, promoting propagation through the matrix, along interfaces or around particles. In ES15 without membrane, particle-rich regions and distinct particle–matrix boundaries are visible. Relatively clean, particle-shaped cavities are consistent with local debonding and pull-out, whereas matrix remnants on particles suggest stronger local anchoring. Fracture remains predominantly brittle, with mixed propagation paths involving fragmentation, interfacial separation, crack deflection and branching.

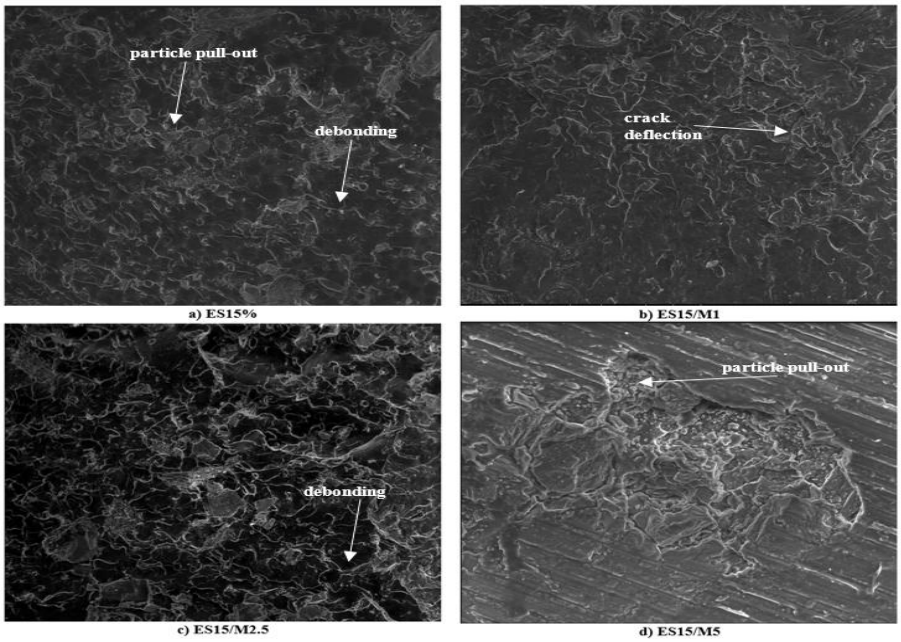


Fig. 10 SEM fracture surfaces of the ES15 series: (a) without membrane, (b) 1 wt%, (c) 2.5 wt% and (d) 5 wt% membrane

The CES15 series exhibits rough, granular particle-rich regions that may promote mechanical interlocking and increase crack-path tortuosity. In CES15 without membrane, cracks change direction near the treated particles. Interfacial gaps suggest local debonding, whereas attached matrix fragments indicate a local cohesive fracture component. Fracture remains mixed and predominantly brittle, with crack deflection and branching influenced by particle geometry and roughness.

At 1% membrane, dispersed powder-rich regions disrupt crack propagation. At 2.5%, large, internally rough agglomerates appear in the selected fracture fields, unlike the polished section in Fig. 8. This difference highlights local variability and prevents ranking agglomeration from individual fields. Agglomerates may deflect or obstruct cracks, but abrupt stiffness changes and uneven bonding at their boundaries may also favour crack initiation, debonding and interfacial propagation. Both formulations therefore retain predominantly brittle fracture, with additional mechanisms of crack deflection, particle pull-out and branching.

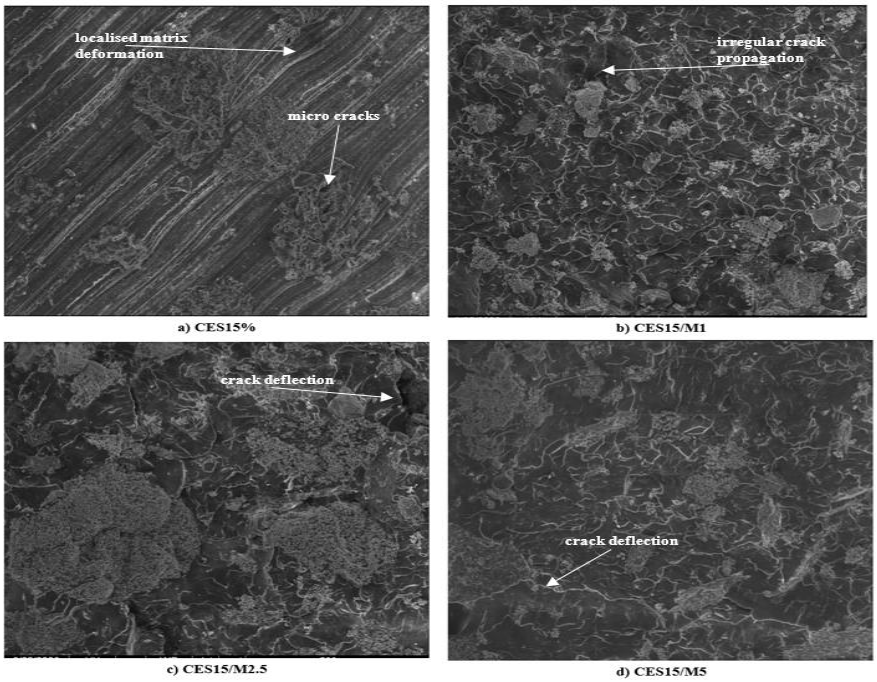


Fig. 11 SEM fracture surfaces of the CES15 series: (a) without membrane, (b) 1 wt%, (c) 2.5 wt% and (d) 5 wt% membrane

At 5% membrane, agglomerates remain present but are separated by larger matrix regions. The crack therefore propagates through a succession of filler-rich and filler-poor regions. This heterogeneity may cause both crack deflection and local stress concentrations. Compared with the ES15 series, the CES15 particles are morphologically more distinct and rougher, but the potential advantage of mechanical interlocking may be reduced when agglomeration or interfacial voids predominate. At 5% membrane, the mechanism remains mixed and predominantly brittle; the alternation between filler-rich zones and matrix regions produces a discontinuous and irregular crack path. Excessive agglomeration may reduce the benefit of mechanical interlocking because it introduces heterogeneities and local stress concentrators.

Comparison of the images shows a transition from predominantly brittle matrix fracture in REF to a mixed mechanism in the composites. The powder introduces interfaces that can locally arrest or deflect the crack but also defects that may become crack-initiation sites. A cavity with an outline similar to that of a particle is consistent with particle pull-out, whereas a gap at the

particle-matrix boundary indicates debonding. Pores or air bubbles generally have a more rounded geometry and should not automatically be confused with pull-out voids. Both pores and interfacial voids can concentrate stresses and shorten the distance required for microcrack coalescence. In comparative terms, the three systems can be described as follows: REF - predominantly brittle matrix fracture, with cohesive propagation and local branching; ES15 - mixed, predominantly brittle fracture, controlled by the matrix and the particle-matrix interface, with debonding and particle pull-out in certain regions; CES15 - mixed, predominantly brittle fracture, but with more pronounced crack deflection around rough particles and agglomerates as a consequence of the topography induced by thermal treatment.

Overall, the SEM morphology indicates that the fracture mechanism is simultaneously controlled by matrix cohesion, particle-matrix adhesion, degree of agglomeration, and the presence of pores/voids. The effect of the membrane depends on its concentration: small amounts may favourably modify the crack path and local contact, whereas higher levels may increase heterogeneity and agglomeration. Thermal treatment makes the particles rougher and more morphologically distinct, but interfacial performance must be evaluated together with particle distribution and the observed defect density. From the perspective of crack initiation, pores and air bubbles represent important pre-existing defects: at their edges, the load-bearing cross-section is reduced, local stress increases, and a microcrack may form. Subsequently, this microcrack may propagate toward a particle-matrix interface, a pull-out void, or an agglomerate. Overall, the images support predominantly brittle fracture for all three categories, with a more evident mixed contribution in the ES15 and CES15 composites due to crack deflection, branching, and interfacial mechanisms.

3.4. Local mechanical response

Five indentations were performed for each system (Resin, ES, ES+M, CES and CES+M), and the reported values are averages. Measurements targeted microscopically identified reinforcement-associated regions, using a maximum load selected to limit neighbouring-phase contributions. Hardness (HIT) and indentation modulus (EIT) therefore characterize local nanomechanical behaviour rather than bulk composite properties. Representative load–displacement curves are shown in Fig. 12.

The unfilled resin shows the most compliant response and greatest penetration depths, with EIT = 4.16 ± 0.76 GPa and HIT = 153 ± 34 MPa. Native eggshell regions exhibit the stiffest response, with EIT = 33.0 ± 2.55 GPa and HIT = 1274 ± 396 MPa (Table 3), approximately eight times the matrix modulus. The hardness scatter indicates local heterogeneity. The resin indentation modulus is about twice its tensile modulus (2.03 GPa, Table 4), potentially reflecting creep during the hold, pile-up and differences in strain rate. Conversely, the modulus of native filler-associated regions is below values generally reported for calcite and eggshell, suggesting a contribution from the surrounding matrix.

Table 3 Indentation hardness and indentation modulus measured on filler-associated regions

Material	H_{IT} (MPa)	E_{IT} (GPa)
Resin (unfilled matrix)[a]	153 ± 34	4.16 ± 0.76
ES (native eggshell)	1274 ± 396	33.0 ± 2.55
ES+M (native + membrane)	1099 ± 134	29.0 ± 3.16
CES (calcined eggshell)	257 ± 41	8.30 ± 0.94
CES+M (calcined + membrane)	188 ± 32	8.60 ± 0.89

[a]The values for the unfilled resin were obtained on matrix regions of the reference specimen.

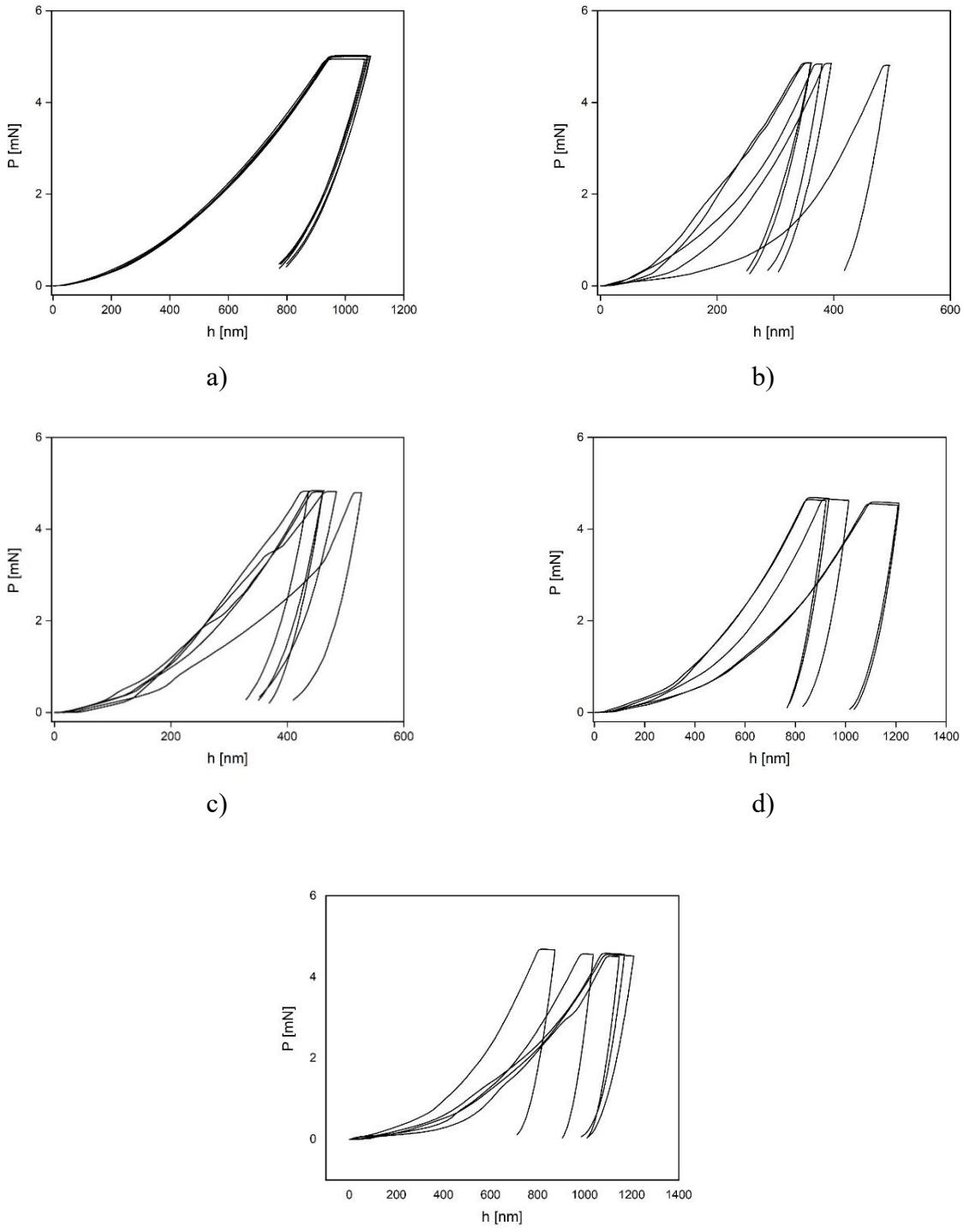


Fig. 12 Representative nanoindentation load-displacement curves for (a) the resin and for the regions associated with (b) ES, (c) ES+M, (d) CES and (e) CES+M

The ES+M system exhibited a mean indentation modulus of 29.0 ± 3.16 GPa and hardness of 1099 ± 134 MPa, both moderately lower than those of ES. Because indentation targeted reinforcement-associated regions, these differences reflect variations in the local micromechanical environment rather than an established change in the intrinsic properties of the mineral phase. Calcination was associated with a substantial reduction in the local nanomechanical response. CES exhibited an indentation modulus of 8.30 ± 0.94 GPa and hardness of 257 ± 41 MPa,

remaining above the matrix values but markedly below those of ES. The fragmented, rougher and porous morphology observed by SEM is consistent with this reduction. The measured response therefore likely reflects contributions from both mineral phase composition and the microstructural architecture developed during thermal treatment.
For CES+M, the indentation modulus remained comparable to CES at 8.6 ± 0.9 GPa, whereas the mean hardness decreased to 188 ± 32 MPa. Membrane incorporation thus produced a larger relative change in hardness than in modulus, suggesting that the calcined filler structure remained the principal influence on local stiffness.
Overall, the measurements distinguish three levels of local stiffness: approximately 4 GPa for the PMMA matrix, 8–9 GPa for calcined filler-associated regions and 29–33 GPa for native filler-associated regions. Calcination was associated with the largest differences in local stiffness and hardness, while the effects of membrane incorporation were comparatively modest.

3.5. Tensile behaviour

Tensile modulus and strength are listed in Table 4; representative curves are shown in Fig. 13, the trends with mineral content in Fig. 14 and the energy to fracture in Fig. 15.

Table 4 Tensile modulus and strength of the thirteen investigated formulations

Formulation	E (MPa)	σ (MPa)
REF	2027 ± 166	29.4 ± 3.0
ES5	2450 ± 146	29.3± 1.1
ES10	2627 ± 153	29.4± 1.7
ES15	2646 ± 121	30.0 ± 1.7
ES15/M1	2414 ± 126	22.9 ± 1.7
ES15/M2.5	2700 ± 98	24.3 ± 1.3
ES15/M5	2814 ± 233	23.8 ± 0.7
CES5	2423 ± 131	31.8 ± 1.6
CES10	2798 ± 360	30.4 ± 4.1
CES15	2934 ± 517	25.9 ± 1.9
CES15/M1	3003 ± 50	27.2 ± 5.0
CES15/M2.5	3025 ± 317	28.2 ± 2.4
CES15/M5	3375 ± 338	24.7 ± 3.2

Every filled formulation had a higher mean modulus than the reference (2027), by 19% (ES15/M1) to 67% (CES15/M5, 3375). The native series rose from 2450 MPa at ES5 to 2646 MPa at ES15 and the calcined series from 2423 to 2934 MPa, with large scatter at CES10 and CES15. Mean strength changed little in the native series (29.3–30.0 MPa against 29.4 MPa), fell from 31.8 to 25.9 MPa across CES5–CES15 and dropped to 22.9–24.3 MPa in the membrane-bearing native formulations, so that 78–108% of the reference strength was retained. This divergence between stiffness and strength is the usual signature of a rigid filler that stiffens the matrix while transmitting little tensile load across the interface [25, 37].
In statistical design A neither mineral loading ($p = 0.690$) nor mineral state ($p = 0.688$) affected the modulus significantly. In statistical design B mineral state was the only significant factor ($F(1,12) = 15.87$, $p = 0.002$, partial $\eta^2 = 0.569$), with membrane content ($p = 0.134$) and the interaction ($p = 0.691$) not significant. One-way analysis found an overall formulation effect on modulus ($F(10,18) = 2.60$, $p = 0.037$), but only CES15/M5 differed from REF in Tukey testing. For strength, no factor was significant in either design, and the one-way effect ($F(10,18) = 2.92$, $p = 0.023$) did not resolve into any significant pair.

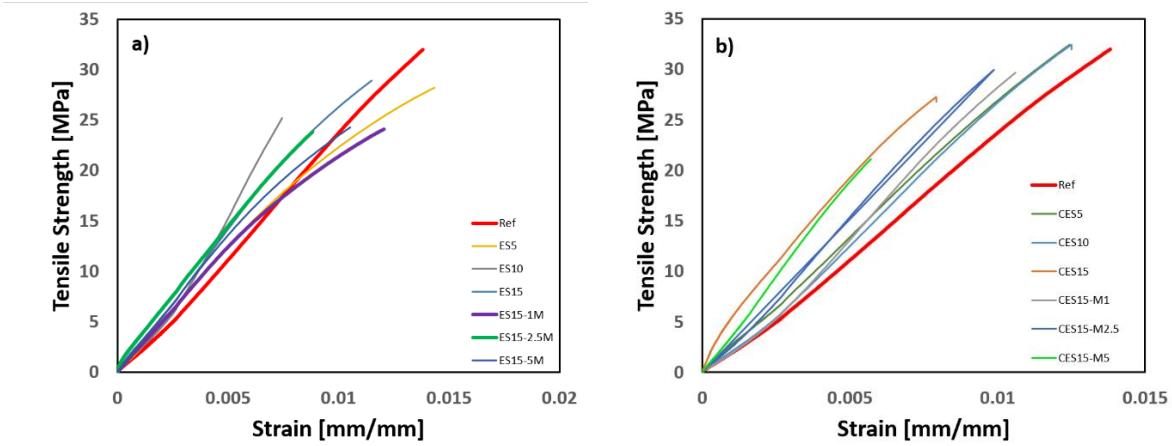


Fig. 13 Representative tensile stress-strain curves: (a) the ES series and (b) the CES series

At 15 wt% mineral the calcined composites were stiffer than the native ones at every membrane level, by 288–589 MPa (2934 against 2646 MPa without membrane). They achieved this at a lower filler volume fraction, yet calcination also changes morphology and porosity, so the comparison does not isolate phase chemistry.

The closest literature comparison is the self-curing acrylic study of Mohammed [30], who used eggshell powder before and after burning at 700 °C for 2 h. Between 1 and 7 wt%, tensile strength rose there from 56.0 to 67.3 MPa for the untreated and from 59.0 to 72.0 MPa for the burned powder, and the modulus from 2.23 to 3.27 GPa and from 2.83 to 4.27 GPa. Both studies find the thermally treated powder stiffer, and they disagree on strength. Mohammed's powders averaged 15 µm before and 10 µm after burning, and the strength gain was attributed to the large interfacial area of such fine particles. The burning also gave 89% CaO by X-ray fluorescence against complete conversion here. Particle size is therefore a likely variable separating a strengthening eggshell filler from an extending one.

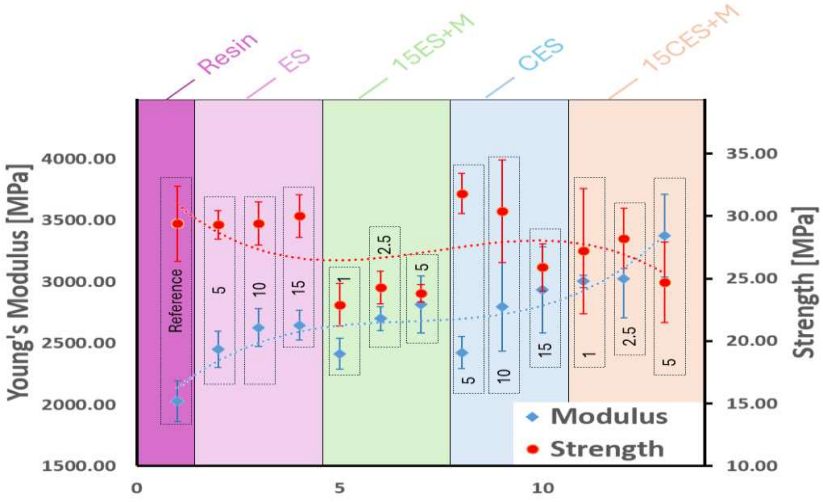


Fig. 14 Tensile modulus and tensile strength against mineral content for the ES and CES series, with error bars

The energy absorbed to fracture (Fig. 15) separated the formulations most sharply ($F(10,18) = 6.68$, $p < 0.001$, $\eta^2 = 0.788$). No formulation reached the reference value of 0.22 ± 0.01 MJ m^{-3}, with ES15 that absorbed 0.17 ± 0.02, CES15 0.10 ± 0.01 and CES15/M5 0.08 ± 0.03 MJ m^{-3}, the last being 39% of the reference, and ES15/M1, ES15/M2.5, ES15/M5, CES15 and CES15/M5 differed significantly from REF.

The ranking of the two minerals was not constant. CES absorbed as much energy as ES or more at 5 and 10 wt% and at 1 and 2.5 wt% membrane, and less at 15 wt% and at 5 wt% membrane. CES15/M5 combined the highest stiffness with reduced strength and the lowest energy, as expected for a filler that rigidifies the matrix locally while adding crack-initiation sites.

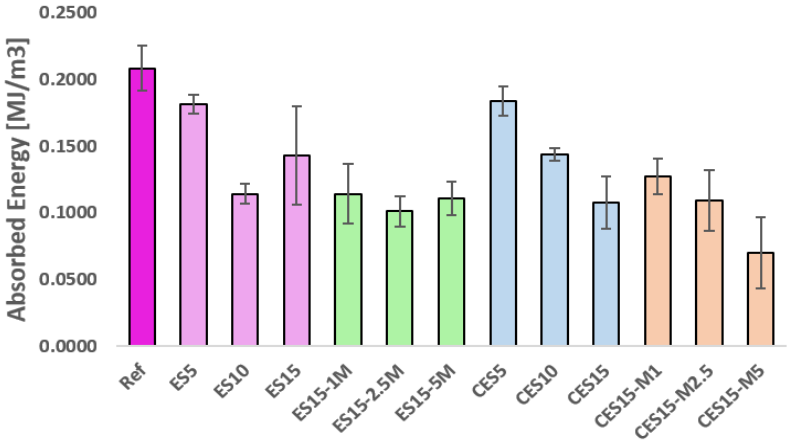


Fig. 15 Energy absorbed to fracture in tension for all formulations

3.6. Flexural behaviour

All flexural specimens fractured in a brittle manner before the end of the test (Fig. 16). Because most fractures occurred below 3.5% strain, the ISO 178 flexural strength at break σ_{fM} was used for all formulations, including the reference, which broke at 4.20% (Table 5).

Bending was the most severely degraded loading state. Flexural strength fell from 87.1 MPa for REF to 47.6, 43.0 and 40.4 MPa at ES5, ES10 and ES15, and the strain at fracture from 4.20 to 2.12%. CES15 had the same strength, 40.4 MPa, at the lowest fracture strain of the set (1.91%), and the membrane levels on the native base spanned 33.7–41.8 MPa without trend. Every filled formulation retained only 39–55% of the reference strength and was significantly below it ($F(8,18) = 23.48$, $p < 0.001$, $\eta^2 = 0.913$).

Table 5 Flexural properties

Formulation	σ_{fM} (MPa)	ε_{fM} (%)	E_f (MPa)	EA_{tot} (MJ m^{-3})
REF	87.1 ± 5.6	4.20 ± 0.60	2605 ± 330	2.10 ± 0.37
ES5	47.6 ± 12.8	3.07 ± 0.39	1663 ± 352	0.80 ± 0.31
ES10	43.0 ± 3.7	2.45 ± 0.39	2101 ± 166	0.59 ± 0.14
ES15	40.4 ± 6.6	2.12 ± 0.08	2238 ± 449	0.47 ± 0.06
ES15/M1	33.7 ± 0.7	2.26 ± 0.28	1867 ± 323	0.43 ± 0.05
ES15/M2.5	41.0 ± 3.0	2.21 ± 0.06	2107 ± 118	0.49 ± 0.03
ES15/M5	41.8 ± 4.5	2.54 ± 0.26	1886 ± 411	0.57 ± 0.01
CES15	40.4 ± 2.4	1.91 ± 0.08	2248 ± 35	0.40 ± 0.04
CES15/M2.5	38.7 ± 1.2	2.01 ± 0.11	2116 ± 179	0.41 ± 0.03

The severity of the loss reflects the stress state. In three-point bending the maximum tensile stress acts on the outer surface, where casting flash, near-surface voids and agglomerates are sampled preferentially. The realised span-to-thickness ratio ranged from 15.3 to 19.9 against the ISO target of 16 ± 1. Because stress is calculated with the measured thickness of each specimen, σ_{fM} is not biased directly, and L/h did not differ between formulations ($F(8,18) = 1.77$, $p = 0.149$), although it probably adds scatter. All filled formulations also had a lower

mean flexural modulus than REF (1663–2248 against 2605 MPa), opposite to the tensile trend. This modulus effect was marginal ($p = 0.049$, only ES5 below REF), so the tensile modulus remains the principal stiffness metric.

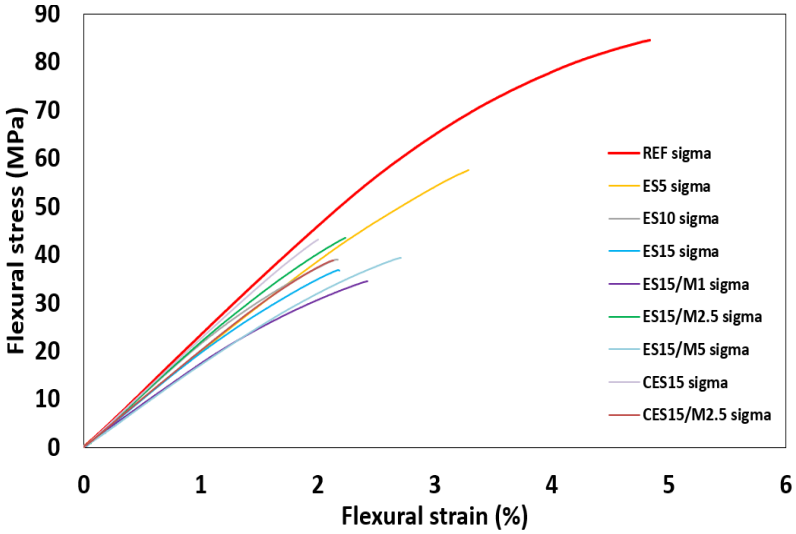


Fig. 16 Representative flexural stress–strain curves to fracture

Flexural energy absorption fell from 2.10 MJ m^{-3} for REF to 0.80, 0.59 and 0.47 MJ m^{-3} at ES5, ES10 and ES15 and to 0.40–0.41 MJ m^{-3} for the calcined formulations, 19–22% of the reference at 15 wt% ($F(8,18) = 30.01$, $p < 0.001$, $\eta^2 = 0.930$). In statistical design C mineral state was the only significant factor for the absorbed energy, which was lower for the calcined composites ($F(1,8) = 9.09$, $p = 0.017$, partial $\eta^2 = 0.532$), while neither factor affected flexural strength ($p \geq 0.628$). Membrane content produced no systematic recovery of energy absorption (Fig. 17).

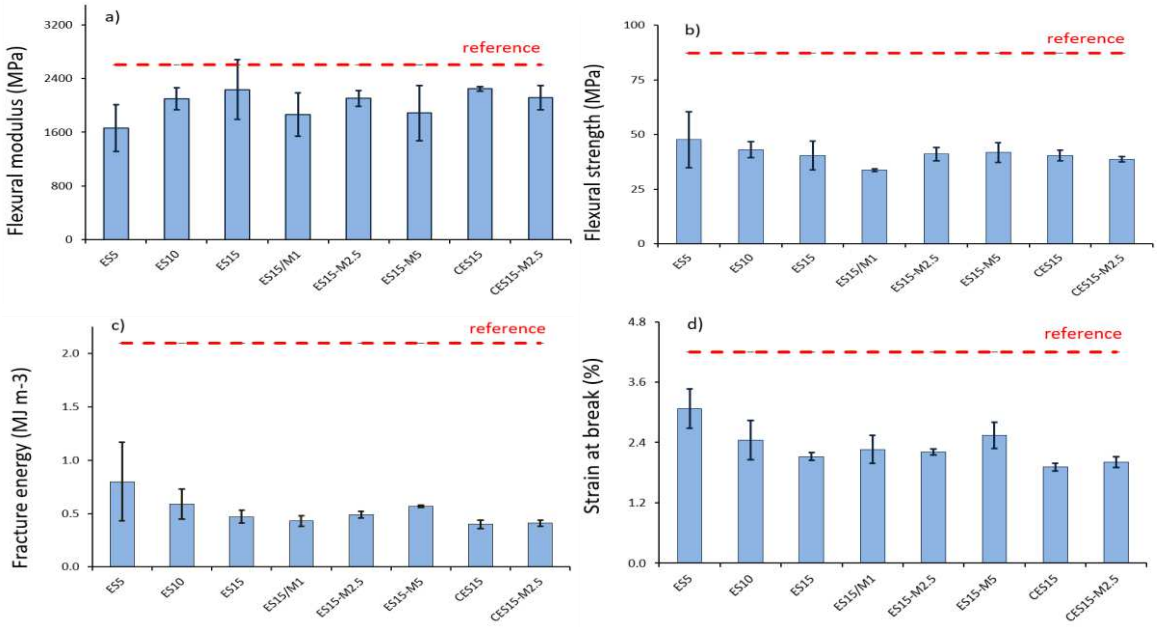


Fig. 17 Flexural properties by formulation, (a) Modulus, (b) Strength, (c) Absorbed Energy and (d) Strain at break

3.7. Compression and porosity

Compression curves exhibited the expected rise to yield, plateau and densification stages and the first local maximum was used as yield stress (Table 6).

Table 6 Compressive yield stress and porosity determined on the cylindrical compression specimens

Formulation	σ_{yield} (MPa)	Apparent porosity (%)
REF	103.2 ± 10.2	2.22 ± 0.6
ES15	108.1 ± 3.6	1.28 ± 0.85
ES15/M1	111.2 ± 1.4	2.97 ± 0.67
ES15/M2.5	110.6 ± 1.6	2.77 ± 0.6
ES15/M5	103.7 ± 3.7	3.94 ± 2.03
CES15	103.2 ± 8.7	7.28 ± 0.7
CES15/M2.5	106.6 ± 3.5	5.75 ± 0.6

Compressive yield stress remained at 100–108% of REF for all tested formulations, and the differences were not significant ($F(6,12) = 1.39$, $p = 0.294$). Group means of the compressive modulus lay between 953 and 1413 MPa with large scatter, and the energy absorbed to yield between 5.5 and 7.1 MJ m^{-3} (Fig. 18).

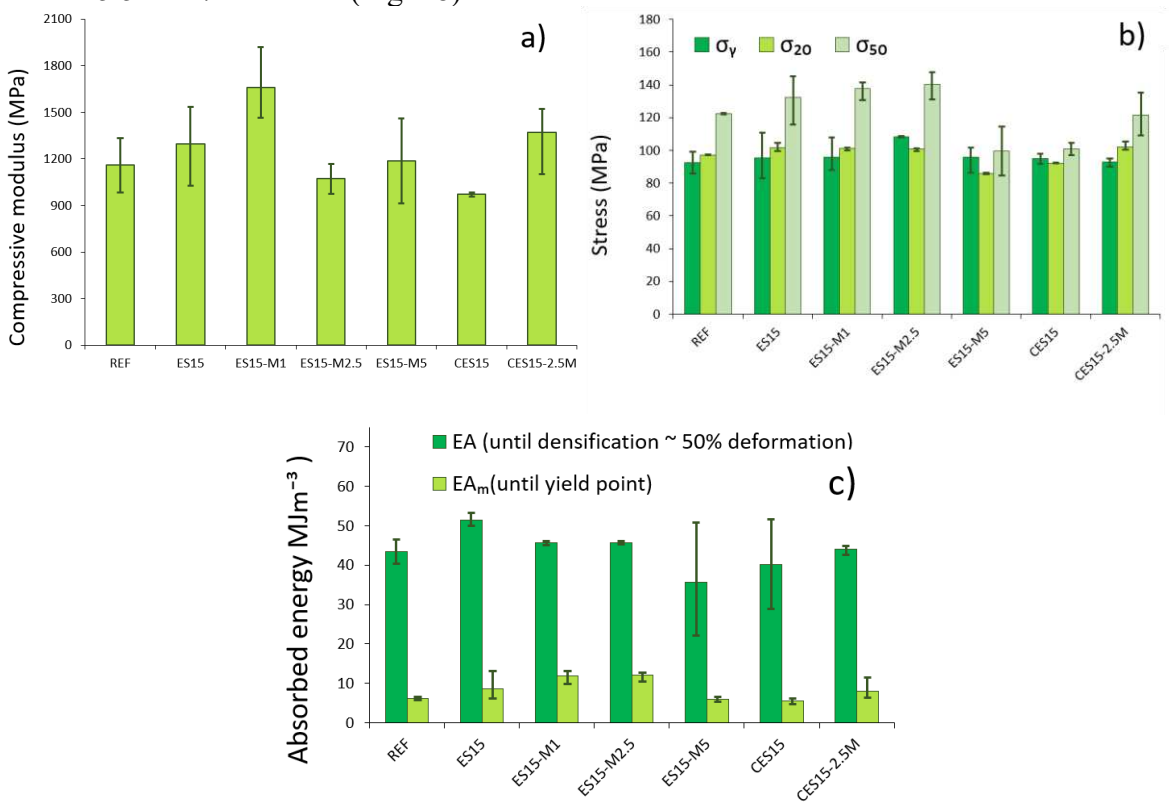


Fig. 18 Compressive properties: (a) compressive modulus, (b) stress at the yield point, at 20 % deformation and at 50 % deformation and (c) energy absorbed up to the yield point

Compression is the only loading state in which the composites kept the performance of the reference (representative curves in Fig. 19). Under compression a debonded interface opens no crack, so a poorly bonded rigid particle still carries load, whereas in tension the same interface becomes a crack-initiation point or area.

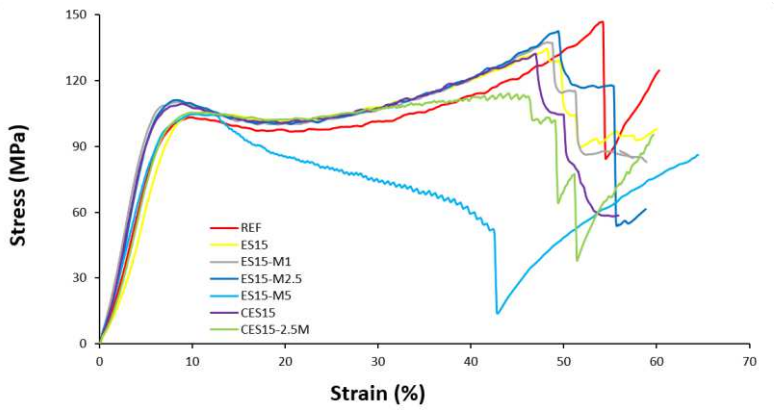


Fig. 19 Representative compressive stress–deformation curves

Apparent porosity (Table 6 and Fig. 20) was the largest and most systematic difference between the two formulations: REF gave 2.2%, the native formulations 1.3–3.9%, and CES15 and CES15/M2.5 reached 7.3 ± 0.7% and 5.7 ± 0.6%. Formulation had a strong effect ($F(6,13) = 12.38$, $p < 0.001$, $\eta^2 = 0.851$). CES15 was more porous than REF and every native formulation, and CES15/M2.5 more porous than REF, ES15 and ES15/M2.5. In statistical design D, mineral state gave the largest effect measured in this work ($F(1,8) = 123.03$, $p < 0.001$, partial $\eta^2 = 0.939$). The significant state × membrane interaction ($p = 0.006$) reflects opposite membrane effects, which lowered the porosity of CES15 from 7.3 to 5.7% and raised that of ES15 from 1.3 to 2.8%.

The small within-group scatter shows a systematic effect, and together with the portlandite found by XRD it points to a mechanism tied to the calcined filler. Three contributions are possible. The theoretical density of the calcined formulations uses the density of CaO, whereas part of the filler is less dense portlandite and for a fully hydrated filler the porosity of CES15 would fall from 7.3 to about 4.6%, still well above the native equivalent. The porous calcined aggregates may also be incompletely infiltrated during the short working time. Finally, the basic, hygroscopic surface of CES and the heat of its hydration may disturb the peroxide–amine cure locally. Separating these requires the $CaO/Ca(OH)_2$ ratio and sections through the calcined aggregates. For a cast-in-place process, the calcined filler carries a porosity penalty that the native powder avoids.

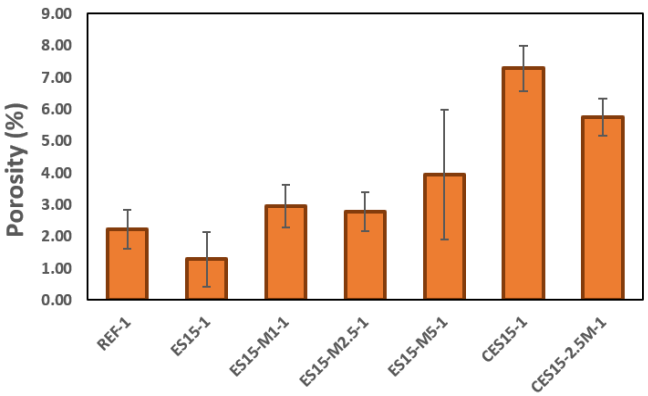


Fig. 20 Apparent porosity of the seven-compression formulations determined from cylinder mass and measured volume, with error bars

3.8. Statistical summary

Table 7 collects the two-factor analyses cited in Sections 3.5–3.7, and Fig. 21 shows the tensile modulus of all formulations. Mineral state produced the two largest effects, on apparent

porosity in design D (partial $\eta^2 = 0.939$) and on tensile modulus in design B (partial $\eta^2 = 0.569$), and it was also significant for flexural fracture energy in design C. No factor or interaction reached significance for tensile strength, flexural strength or compressive yield stress.

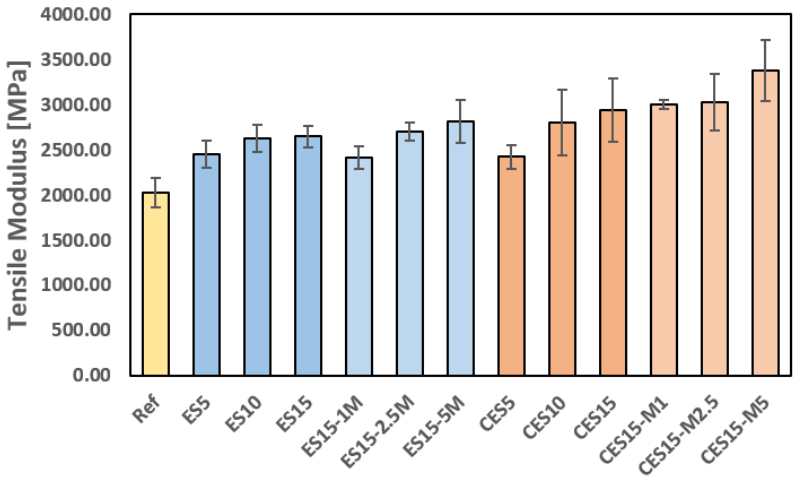


Fig. 21 Tensile modulus of all formulations

Table 7 Two-factor analyses of variance (type III sums of squares)

Design	Response	Factor	df	F	p	partial η^2
A	Tensile modulus	Mineral state	1	0.18	0.688	0.024
A	Tensile modulus	Mineral loading	2	0.39	0.690	0.101
A	Tensile modulus	State × loading	2	0.08	0.928	0.021
A	Tensile strength	Mineral state	1	0.02	0.900	0.002
A	Tensile strength	Mineral loading	2	1.08	0.390	0.236
A	Tensile strength	State × loading	2	1.71	0.248	0.329
B	Tensile modulus	Mineral state	1	15.87	0.002	0.569
B	Tensile modulus	Membrane content	3	2.26	0.134	0.361
B	Tensile modulus	State × membrane	3	0.50	0.691	0.111
B	Tensile strength	Mineral state	1	1.02	0.332	0.079
B	Tensile strength	Membrane content	3	1.63	0.235	0.289
B	Tensile strength	State × membrane	3	2.37	0.122	0.372
C	Flexural strength	Mineral state	1	0.25	0.628	0.031
C	Flexural strength	Membrane content	1	0.06	0.815	0.007
C	Flexural strength	State × membrane	1	0.25	0.630	0.030
C	Flexural modulus	Mineral state	1	0.00	0.949	0.001
C	Flexural modulus	Membrane content	1	0.83	0.389	0.094
C	Fracture energy	Mineral state	1	9.09	0.017	0.532
C	Fracture energy	Membrane content	1	0.37	0.562	0.044
C	Fracture energy	State × membrane	1	0.03	0.868	0.004
D	Compressive yield stress	Mineral state	1	2.84	0.136	0.289
D	Compressive yield stress	Membrane content	1	1.24	0.302	0.151
D	Compressive yield stress	State × membrane	1	0.02	0.886	0.003
D	Porosity	Mineral state	1	123.03	< 0.001	0.939
D	Porosity	Membrane content	1	0.00	0.955	0.000
D	Porosity	State × membrane	1	13.96	0.006	0.636

3.9. Multiscale interpretation and reference models

The tensile data were compared against two limiting descriptions. For the modulus, the Guth reference prediction for rigid spherical inclusions [38],

$$E_c = E_m(1 + 2.5\varphi + 14.1\varphi^2) \quad (15)$$

serves as a simplified reference for the stiffening expected from rigid particulate inclusions at the nominal volume fraction; deviations from it must be interpreted with caution, because particle shape, agglomeration, porosity and the uncertainty in the effective filler volume are not represented. For the strength, the Nicolais–Narkis expression:

$$\sigma_c = \sigma_m(1 - 1.21\varphi 2/3) \quad (16)$$

describes the limiting case of non-adhering inclusions, in which the particles act as voids [28, 29]. The ratios of the measured to the predicted values are given in Table 9.

Measured-to-predicted strength ratios were 1.01–1.29 with a mean of 1.15 (Table 8), so every composite lies at or moderately above the prediction for non-adhering inclusions. The excess suggests some stress transfer, but it is small, since no filled formulation exceeds the strength of the unfilled resin significantly. Because the particles are irregular, broadly sized and partly agglomerated, the expression is used as a reference description and does not measure adhesion directly.

Table 8 Measured tensile modulus and strength expressed as ratios to the Guth and Nicolais–Narkis predictions. A strength ratio of unity indicates behaviour identical to that of non-adhering inclusions. Reference values: Em = 2027 MPa and σm = 29.4 MPa

Formulation	φ	E measured / Guth	σ measured / Nicolais–Narkis
ES5	0.022	1.14	1.10
ES10	0.046	1.13	1.18
ES15	0.071	1.05	1.29
ES15/M1	0.081	0.92	1.01
ES15/M2.5	0.096	0.97	1.11
ES15/M5	0.122	0.92	1.15
CES5	0.018	1.14	1.18
CES10	0.038	1.24	1.20
CES15	0.059	1.21	1.08
CES15/M1	0.069	1.20	1.16
CES15/M2.5	0.084	1.14	1.25
CES15/M5	0.109	1.16	1.16

The modulus ratios separated the two mineral states. In the native series the ratio fell with loading, from 1.14 at ES5 to 1.05 at ES15 and 0.92 at ES15/M1 and ES15/M5, a growing shortfall against the geometric prediction. In the calcined series it stayed between 1.14 and 1.24, above the stiffening expected from rigid spheres at the same nominal volume fraction. Part of this excess may come from the CES volume fraction, which is calculated with the density of CaO. Porosity thus widens the gap between the two formulations, and the higher stiffness of the calcined composites cannot come from a higher intrinsic filler modulus. Three mechanisms are plausible: constraint of matrix mobility by the irregular, fragmented calcined surfaces; modification of the matrix next to a reactive filler and an effective filler volume larger than the nominal one, because the porous aggregates are only partly infiltrated and part of the filler is less dense portlandite. The present data cannot separate them, and this inversion is the

principal open question of the work. Porosity must therefore be treated as a covariate whenever the formulations are compared.

3.10. Implications for waste valorisation

Native and calcined eggshell are not equivalent formulations for waste valorisation. Calcination at 900 °C adds a high-temperature step, releases about 0.44 kg of CO_2 per kg of carbonate decomposed and yields a filler whose phase composition changes during storage. Its measurable benefit here is a higher tensile modulus, obtained together with higher porosity and lower flexural energy. The native powder needs only washing, drying and grinding; at 5 wt% it raised the mean tensile modulus by 21% without loss of tensile strength, and at 15 wt% it preserved the compressive yield stress. For cast-in-place parts loaded mainly in compression, the native powder is the better one, and calcination is justified only where extra stiffness is required. A life-cycle assessment would be needed to quantify this advantage. Where flexural strength or energy absorption governs, none of the formulations is suitable without modification of the interface.

4. Conclusions

Calcination at 900 °C for 3 h converts the calcite of hen eggshell into CaO, part of which rehydrates to portlandite. The native and calcined fillers are therefore distinct mineral systems, and equal mass fractions are not iso-volumetric.

Nanoindentation resolves 4.16 ± 0.76 GPa for the matrix, 33.0 ± 2.55 GPa for native-filler-associated regions and 8.30 ± 0.94 GPa for calcined-filler-associated regions. Calcination reduces the local modulus fourfold, consistent with its fragmented, porous particle architecture.

All filled formulations were stiffer in tension than the matrix, by 19–67%, and at 15 wt% the calcined composites were significantly stiffer than the native ones despite their lower local stiffness and higher porosity.

The calcined formulation raised the apparent porosity of the 15 wt% composite to 7.3 ± 0.7% against 1.3 ± 0.9% for the native equivalent, the largest effect measured. Portlandite density, incompletely infiltrated aggregates and local cure effects may all contribute, and porosity has to be reported alongside any interfacial interpretation.

Tensile strength stayed within 1.01–1.29 times the Nicolais–Narkis prediction for non-adhering inclusions, indicating limited interfacial stress transfer. The composites retained 39–55% of the flexural strength, 78–108% of the tensile strength and 100–108% of the compressive yield stress, while flexural energy fell by up to 81%. The membrane, at up to 5 wt%, did not change the tensile modulus significantly and behaved as a compliant filler.

Eggshell-derived powders in a cold-cured acrylic are best regarded as functional fillers that keep compressive performance, at the cost of flexural strength and fracture energy when no coupling agent is used. The native powder is the more favourable choice, since calcination adds an energy-intensive step and a porosity penalty for a benefit limited to stiffness.

Statements and Declarations

Funding

The authors did not receive support from any organization for the submitted work.

Competing Interests

The authors have no relevant financial or non-financial interests to disclose.

Author Contributions

Iasmina-Mădălina Petculescu: Conceptualization, Methodology, Writing – original draft. Carmen Opriș: Formal analysis, Investigation, Writing – review and editing, Supervision. Dragoș Buzdugan: Formal analysis, Investigation, Writing – review and editing, Supervision. Maria Rada: Writing – review and editing, Supervision. Dragoș-Ion Uțu: Writing – review and editing, Supervision. Alexandru-Viorel Coșa: Conceptualization, Methodology, Formal analysis, Investigation, Writing – original draft, review and editing.

Data Availability

The raw data supporting the findings of this study are available in the Mendeley Data repository: Cosa, Alexandru-Viorel (2026), "Eggshell_Paper_Test_Data_Raw", Mendeley Data, V1, https://doi.org/10.17632/jbkx7kmnsw.1.

References

1.Vandeginste V (2021) Food waste eggshell valorization through development of new composites: A review. Sustain Mater Technol 29:e00317. https://doi.org/10.1016/j.susmat.2021.e00317

2.Owuamanam S, Cree D (2020) Progress of Bio-Calcium Carbonate Waste Eggshell and Seashell Fillers in Polymer Composites: A Review. J Compos Sci 4:70. https://doi.org/10.3390/jcs4020070

3.Han C et al (2023) Advances in eggshell membrane separation and solubilization technologies. Front Vet Sci 10:1116126. https://doi.org/10.3389/fvets.2023.1116126

4.Shanmugam V et al (2021) Circular economy in biocomposite development: State-of-the-art, challenges and emerging trends. Compos Part C Open Access 5:100138. https://doi.org/10.1016/j.jcomc.2021.100138

5.Razali R, Musa FA, Jumadi N, Jalani AY (2021) Production of Calcium Oxide from Eggshell: Study on Calcination Temperature, Raw Weight and Contact Time. RSU International Research Conference. pp 624–637

6.Tangboriboon N, Kunanuruksapong R, Sirivat A (2012) Preparation and properties of calcium oxide from eggshells via calcination. Mater Sci-Pol 30:313–322. https://doi.org/10.2478/s13536-012-0055-7

7.Mustapha K, Ayinla R, Ottan AS, Owoseni TA (2020) Mechanical properties of calcium carbonate/eggshell particle filled polypropylene composites. MRS Adv 5:2783–2792. https://doi.org/10.1557/adv.2020.323

8.Farm YY et al (2022) Mechanical properties of eggshells powder reinforced recycled high-density polyethylene. IOP Conf Ser Mater Sci Eng 1217:012003. https://doi.org/10.1088/1757-899X/1217/1/012003

9.Skórczewska K et al (2022) Waste Eggshells as a Natural Filler for the Poly(Vinyl Chloride) Composites. Polymers 14:4372. https://doi.org/10.3390/polym14204372

10.Cree D, Owuamanam S, Soleimani M (2023) Mechanical Properties of a Bio-Composite Produced from Two Biomaterials: Polylactic Acid and Brown Eggshell Waste Fillers. Waste 1:740–760. https://doi.org/10.3390/waste1030044

11.Wu H et al (2020) Preparation and Properties of Biocomposite Films Based on Poly(vinyl alcohol) Incorporated with Eggshell Powder as a Biological Filler. J Polym Environ 28:2020–2028. https://doi.org/10.1007/s10924-020-01747-2
12.Sarmin SN et al (2023) The Effect of Eggshell Fillers on the Physical, Mechanical, and Morphological Properties of Date palm Fibre Reinforced Bio-epoxy Composites. J Polym Environ 31:5015–5027. https://doi.org/10.1007/s10924-023-02924-9
13.Intharapat P, Kongnoo A, Kateungngan K (2013) The Potential of Chicken Eggshell Waste as a Bio-filler Filled Epoxidized Natural Rubber (ENR) Composite and its Properties. J Polym Environ 21:245–258. https://doi.org/10.1007/s10924-012-0475-9
14.Bhagavatheswaran ES et al (2019) The Taste of Waste: The Edge of Eggshell Over Calcium Carbonate in Acrylonitrile Butadiene Rubber. J Polym Environ 27:2478–2489. https://doi.org/10.1007/s10924-019-01530-y
15.Sivakumar AA, Sankarapandian S, Avudaiappan S, Flores EIS (2022) Mechanical Behaviour and Impact of Various Fibres Embedded with Eggshell Powder Epoxy Resin Biocomposite. Materials 15:9044. https://doi.org/10.3390/ma15249044
16.Kowshik S et al (2024) Comparative Study of Unhatched and Hatched Chicken Egg Shell-Filled Glass Fibre/Polyester Composites. J Compos Sci 8:432. https://doi.org/10.3390/jcs8100432
17.Cree D, Soleimani M (2023) Bio-Based White Eggshell as a Value-Added Filler in Poly(Lactic Acid) Composites. J Compos Sci 7:278. https://doi.org/10.3390/jcs7070278
18.Homavand A, Cree DE, Wilson LD (2024) Polylactic Acid Composites Reinforced with Eggshell/$CaCO_3$ Filler Particles: A Review. Waste 2:169–185. https://doi.org/10.3390/waste2020010
19.Ray S, Acharya S, Barik PK, Das S (2024) Study on Mechanical Properties of Polymer Composites Filled with Nano Egg-shell Powder. Arch Curr Res Int 24:360–369. https://doi.org/10.9734/acri/2024/v24i5710
20.Skórczewska K, Lewandowski K, Wilczewski S, Szulc J, Rakowska P (2025) Utilization of Ground Eggshell as a Biofiller of Plasticized PVC-Based Materials Fabricated Using Melt Blending. Polymers 17:434. https://doi.org/10.3390/polym17040434
21.Kuciel S, Rusin-Żurek K, Kurańska M (2024) The Influence of Filler Particle Size on the Strength Properties and Mechanical Energy Dissipation Capacity of Biopoly(Ethylene Terephthalate) BioPET/Eggshell Biocomposites. Recycling 9:88. https://doi.org/10.3390/recycling9050088
22.Coșa AV, Linul E, Șerban DA (2026) Flexural performance of mSLA-printed cenosphere-reinforced photopolymer composites. Proc Rom Acad Ser A (in press)
23.Perera YS, Naaib M, Ariyasinghe N, Abeykoon C (2025) Investigation of the effect of extrusion process parameters and filler loading on the performance of LDPE composites reinforced with eggshell powder. Compos Part C Open Access 16:100561. https://doi.org/10.1016/j.jcomc.2025.100561
24.Affdl JCH, Kardos JL (1976) The Halpin-Tsai equations: A review. Polym Eng Sci 16:344–352. https://doi.org/10.1002/pen.760160512
25.Fu S-Y, Feng X-Q, Lauke B, Mai Y-W (2008) Effects of particle size, particle/matrix interface adhesion and particle loading on mechanical properties of particulate–polymer composites. Compos Part B Eng 39:933–961. https://doi.org/10.1016/j.compositesb.2008.01.002
26.Mortazavi B, Baniassadi M, Bardon J, Ahzi S (2013) Modeling of two-phase random composite materials by finite element, Mori–Tanaka and strong contrast methods. Compos Part B Eng 45:1117–1125. https://doi.org/10.1016/j.compositesb.2012.05.015

27.Nath D, Jangid K, Susaniya A, Kumar R, Vaish R (2021) Eggshell derived CaO-Portland cement antibacterial composites. Compos Part C Open Access 5:100123. https://doi.org/10.1016/j.jcomc.2021.100123
28.Nicolais L, Narkis M (1971) Stress-strain behavior of styrene-acrylonitrile/glass bead composites in the glassy region. Polym Eng Sci 11:194–199. https://doi.org/10.1002/pen.760110305
29.Zare Y (2016) Development of Nicolais–Narkis model for yield strength of polymer nanocomposites reinforced with spherical nanoparticles. Int J Adhes Adhes 70:191–195. https://doi.org/10.1016/j.ijadhadh.2016.07.006
30.Mohammed RA (2020) PMMA–eggshell composite preparation and studying mechanical properties as a dental material. J Eng Sustain Dev 24(2):30–47. https://doi.org/10.31272/jeasd.24.2.3
31.Srinath P, Bhagyanathan C, Gottmyers Melwyn J, Sathiyaseelan G (2026) Sustainable Dual-Phase Reinforcement of Recycled Aluminium Alloys Using Eggshell-Derived Calcium Compounds for Enhanced Mechanical and Thermal Properties. J Bio Tribo Corros 12:3. https://doi.org/10.1007/s40735-025-01067-9
32.Oleiwi J, Hamad Q, Kadhim N (2019) Study Compression, Hardness and Density properties of PMMA Reinforced by Natural Powder Used in Denture Base application. Eng Technol J 37:522–527. https://doi.org/10.30684/etj.37.12a.5
33.Hincke MT, Nys Y, Gautron J (2010) The Role of Matrix Proteins in Eggshell Formation. J Poult Sci 47:208–219. https://doi.org/10.2141/jpsa.009122
34.Rønning SB et al (2020) Processed Eggshell Membrane Powder Is a Promising Biomaterial for Use in Tissue Engineering. Int J Mol Sci 21:8130. https://doi.org/10.3390/ijms21218130
35.Kulzer GmbH (2026) Technovit 4004: transparent cold embedding system. Resin datasheet. Kulzer GmbH, Hanau. https://kulzer-technik.com/en-kt/en-kt/products/technovit-4004.html. Accessed 18 Sep 2026
36.Oliver WC, Pharr GM (1992) An improved technique for determining hardness and elastic modulus using load and displacement sensing indentation experiments. J Mater Res 7:1564–1583. https://doi.org/10.1557/JMR.1992.1564
37.Park G, Roy S, Kim JW, Kim HC, Kim J (2026) Sustainable resin development for the strategic upcycling of waste fly ash into high-performance polymer composites. Compos Part C Open Access 20:100718. https://doi.org/10.1016/j.jcomc.2026.100718
38.Guth E (1945) Theory of Filler Reinforcement. J Appl Phys 16:20–25. https://doi.org/10.1063/1.1707495